

# Electronic and Magnetic Properties of $\text{RMnO}_3/\text{AMnO}_3$ Heterostructures

Rong Yu,<sup>1,2</sup> Seiji Yunoki,<sup>3,4</sup> Shuai Dong,<sup>1,2,5</sup> and Elbio Dagotto<sup>1,2</sup>

<sup>1</sup>*Department of Physics and Astronomy, University of Tennessee, Knoxville, TN 37996, USA*

<sup>2</sup>*Materials Science and Technology Division, Oak Ridge National Laboratory, Oak Ridge, TN 37831, USA*

<sup>3</sup>*Computational Condensed Matter Physics Laboratory, RIKEN, Wako, Saitama 351-0198, Japan*

<sup>4</sup>*CREST, Japan Science and Technology Agency (JST), Kawaguchi, Saitama 332-0012, Japan*

<sup>5</sup>*Nanjing National Laboratory of Microstructures, Nanjing University, Nanjing 210093, China*

(Dated: June 25, 2018)

The ground state properties of  $\text{RMnO}_3/\text{AMnO}_3$  (RMO/AMO) heterostructures (with  $\text{R}=\text{La}, \text{Pr}, \dots$ , a trivalent rare-earth cation, and  $\text{A}=\text{Sr}, \text{Ca}, \dots$ , a divalent alkaline cation) are studied using a two-orbital double-exchange model including the superexchange coupling and Jahn-Teller lattice distortions. To describe the charge transfer across the interface, the long-range Coulomb interaction is taken into account at the mean-field level, by self-consistently solving the Poisson's equation. The calculations are carried out numerically on finite clusters. We find that the state stabilized near the interface of the heterostructure is similar to the state of the bulk compound (R, A)MO at electronic density close to 0.5. For instance, a charge and orbitally ordered CE state is found at the interface if the corresponding bulk (R, A)MO material is a narrow-to-intermediate bandwidth manganite. But instead the interface regime accommodates an A-type antiferromagnetic state with a uniform  $x^2 - y^2$  orbital order, if the bulk (R, A)MO corresponds to a wide bandwidth manganite. We argue that these results explain some of the properties of long-period  $(\text{RMO})_m/(\text{AMO})_n$  superlattices, such as  $(\text{PrMnO}_3)_m/(\text{CaMnO}_3)_n$  and  $(\text{LaMnO}_3)_m/(\text{SrMnO}_3)_n$ . We also remark that the intermediate states in between the actual interface and the bulk-like regimes of the heterostructure are dependent on the bandwidth and the screening of the Coulomb interaction. In these regions of the heterostructures, states are found that do not have an analog in experimentally known bulk phase diagrams. These new states of the heterostructures provide a natural interpolation between magnetically-ordered states that are stable in the bulk at different electronic densities.

PACS numbers: 73.20.-r, 73.21.Ac, 75.47.Lx

## I. INTRODUCTION

Modern fabrication technology allows for the growth of multilayer structures that are nearly perfect at the atomic level, namely with minimal roughness, employing a variety of transition metal oxides (TMO). Due to the simultaneous participation of several degrees of freedom in TMO, it is expected that the artificial multilayer structures made of these materials will exhibit much richer physics than in conventional semiconductor heterostructures. Indeed, recent studies have revealed some fascinating phenomena, such as the reconstruction of spin, charge, and orbital orders at the interface.<sup>1,2</sup> Many interesting properties have also been theoretically predicted using a variety of many-body techniques.<sup>3,4,5</sup>

Among the several ongoing efforts, there is a considerable interest in the analysis of  $\text{RMnO}_3/\text{AMnO}_3$  (RMO/AMO) heterostructures, where  $\text{R}=\text{La}, \text{Pr}, \dots$  refers to a trivalent rare-earth, and  $\text{A}=\text{Sr}, \text{Ca}, \dots$  is a divalent alkaline element.<sup>6,7,8,9,10,11,12,13,14</sup> At low temperatures, the bulk RMO is in an A-type antiferromagnetic (A-AFM) state, which is an insulator, whereas the bulk AMO is in a G-type antiferromagnetic (G-AFM) state, that is also an insulator. Upon doping, the alloy  $\text{R}_{1-x}\text{A}_x\text{MnO}_3$  ((R, A)MO) exhibits a variety of states depending on the doping concentration  $x$ , which controls the charge density in the alloy. However, the heterostructure RMO/AMO could potentially behave differently from its parent bulk compounds. For instance, the

transfer of charge through the interface caused by the different Fermi energies, and concomitant different electronic density concentrations, of the superlattice components causes a distribution of charge that it is not homogeneous along the growth direction. Hence, several states may exist in different regions of the heterostructure. While far from the interface the behavior must be similar to the one in the bulk compounds, close to the interface it may occur that phases very different from those of the superlattice components may exist due to the charge leaking through the interfaces. For instance, in the short-period  $\text{LaMnO}_3/\text{SrMnO}_3$  (LMO/SMO) superlattices the regime close to the interface exhibits ferromagnetic (FM) metallic behavior, which is different from either  $\text{LaMnO}_3$  or  $\text{SrMnO}_3$ .<sup>7,10,11,15</sup> More interestingly, as the number of Sr layers exceeds a critical value, the metallic behavior gives way to an insulating one, displaying a metal-to-insulator transition (MIT). This suggests that the electronic reconstruction at the interface has a crucial effect on the physical properties of the heterostructure.<sup>3</sup> Theoretically, considerable progress has been made in describing the ferromagnetism induced by this electronic reconstruction.<sup>6,9,16,17,18,19</sup> A recent study by the authors<sup>14</sup> focused on the MIT in the short-period LMO/SMO superlattices. There, a FM metallic state with a dominant  $3z^2 - r^2$  orbital order was found at the interface. The insulating behavior of the superlattice was explained as induced by Anderson localization of this quasi two-dimensional (2D) FM state. Note

that limited by computing power, most theoretical efforts based on computer simulations concentrate on superlattices with a small number of Sr layers. This is enough to understand the FM in the short-period superlattice, but may not be appropriate to study the properties of longer-period structures. Another limitation is that most theoretical studies focus on the LMO/SMO superlattice. The corresponding bulk compound (La, Sr)MnO<sub>3</sub> (LSMO) is a wide bandwidth manganite. But not much is known about the interfacial state of the RMO/AMO superlattice if (R, A)MO is a narrow or intermediate bandwidth manganite.

In this manuscript, we use the two-orbital double-exchange model for manganites, which has been successfully applied to the study of bulk Mn oxides,<sup>20</sup> to the analysis of RMO/AMO heterostructures. These heterostructures are assumed to be grown along the (0, 0, 1) direction (*c* axis). We here also assume that the length of the heterostructure is long enough that the states at the two ends of the heterostructure resemble their bulk counterparts, i.e., an A-AFM at the RMO side and a G-AFM at the AMO side. This assumption allows us to focus on the only interface present in the heterostructure. By using a relaxation method introduced in the following section, we can obtain the magnetic and electronic properties of the ground state of the heterostructure. Different from previous efforts that concentrated on the FM tendency in short-period superlattices, we find that in the heterostructure considered in this paper the state stabilized at the interface depends on the bandwidth of the corresponding bulk compound (R, A)MO at electronic density close to 0.5. If (R, A)MO is a narrow-to-intermediate bandwidth manganite, a state resembling the well-known CE-state of bulk manganites is found to be stabilized at the interface. Hence our calculations suggest a CE-like interface state in the PrMnO<sub>3</sub>/CaMnO<sub>3</sub> heterostructure.<sup>28</sup> But if (R, A)MO is a wide bandwidth manganite, an A-AFM state is found at the interface instead. This is consistent with recent experimental results on the (LMO)<sub>*n*</sub>/(SMO)<sub>*2n*</sub> superlattices.<sup>13</sup>

In addition, it is important to remark that one of the main results of our study is the observation of states close to the interface that do *not* have an analog in experimentally known bulk phase diagrams. These states arise as interpolations between, e.g., the A-AFM and CE-states that dominate in the bulk and interfaces, respectively. For instance, canting of the spins in the CE zigzag chains creates a novel “canted CE state”. Also the relative spin angle between adjacent CE planes can be different from those observed in the bulk. And in some occasions, arrangements of spins and orbitals were identified that do not have a clear bulk analog in experiments.

This paper is organized as follows. In Sec. II, we introduce the two-orbital model and the numerical method used to obtain the ground state properties of the heterostructure. The results for (R, A)MO corresponding to narrow-to-intermediate bandwidth manganites are presented in Sec. III. Results for (R, A)MO corresponding

to wide-bandwidth manganites are provided in Sec. IV. Finally, in Sec. V a discussion of our results is given, followed by conclusions.

## II. MODEL AND NUMERICAL METHOD

To investigate the physical properties of the RMO/AMO heterostructure described in Sec. I, here the two-orbital model for manganites<sup>20</sup> will be applied. This model has been widely used before to study the properties of bulk manganites, and the following assumptions are also widely accepted: (1) the *t*<sub>2g</sub> electrons are considered as localized and are described as classical spins with magnitude *S* = 3/2; (2) the Jahn-Teller lattice distortions are also assumed to be classical; (3) the Hund coupling between the *t*<sub>2g</sub> and *e*<sub>g</sub> electrons is assumed to be infinitely large so that the *e*<sub>g</sub> spin is always parallel to the localized *t*<sub>2g</sub> spin at the same site. Based on these assumptions, the Hamiltonian that will be applied to the manganite heterostructure reads

$$\begin{aligned}
 H = & - \sum_{\langle i, j \rangle}^{\alpha, \beta} \left( t_{\mathbf{r}}^{\alpha\beta} \Omega_{ij} c_{i\alpha}^\dagger c_{j\beta} + \text{H.c.} \right) + \sum_{\langle i, j \rangle} J_{i,j}^{\text{AF}} \mathbf{S}_i \cdot \mathbf{S}_j \\
 & + \sum_i (\phi_i + W_i) n_i + \lambda \sum_i (Q_{1i} n_i + Q_{2i} \tau_i^x + Q_{3i} \tau_i^z) \\
 & + \frac{1}{2} \sum_i (2Q_{1i}^2 + Q_{2i}^2 + Q_{3i}^2). \tag{1}
 \end{aligned}$$

The first term of Hamiltonian Eq.(1) denotes the two-orbital double-exchange hopping term.  $\alpha$  and  $\beta$  run over the two *e*<sub>g</sub> orbitals  $d_{x^2-y^2}$  (orbital *a*) and  $d_{3z^2-r^2}$  (orbital *b*) of a Mn ion.  $c_{i\alpha}$  ( $c_{i\alpha}^\dagger$ ) annihilates (creates) an *e*<sub>g</sub> electron in orbital  $\alpha$  at site *i* with its spin parallel to the localized *t*<sub>2g</sub> spin at site  $\mathbf{S}_i$ .  $\mathbf{r}$  denotes the exchange direction, giving  $t_x^{aa} = t_y^{aa} = 3t_x^{bb} = 3t_y^{bb} = 3t_0/4$ ,  $t_y^{ab} = t_x^{ba} = -t_x^{ab} = -t_y^{ba} = \sqrt{3}t_0/4$ ,  $t_z^{aa} = t_z^{bb} = t_z^{ba} = 0$  and  $t_z^{bb} = t_0$  ( $t_0$  is set to be the energy unit). The hopping amplitude is affected by the factor  $\Omega_{ij} = \cos(\frac{\theta_i}{2}) \cos(\frac{\theta_j}{2}) + \sin(\frac{\theta_i}{2}) \sin(\frac{\theta_j}{2}) \exp[-i(\varphi_i - \varphi_j)]$ , where  $\theta_i$  and  $\varphi_i$  are the angles of the *t*<sub>2g</sub> spins in spherical coordinates. Here, we will assume that the hopping amplitudes are the same for electrons on both sides of the heterostructure. This may not be realistic given the possible mismatch of lattice constants between the two different compounds. However, since the superexchange coupling is more sensitive to the change of lattice constant than the hopping amplitudes themselves, as a first approximation we assume that the hopping constants keep the same value on both sides while the superexchange couplings may become layer dependent. The second term is the standard superexchange interaction between nearest-neighbor (NN) *t*<sub>2g</sub> spins. Here the *t*<sub>2g</sub> spin  $\mathbf{S}_i = (\sin \theta_i \cos \varphi_i, \sin \theta_i \sin \varphi_i, \cos \theta_i)$  has been normalized to a unit vector (the actual *S*=3/2 magnitude of

the spins is absorbed in the superexchange coupling). To consider the effect of possible distortions from a perfect cubic lattice, two couplings are used:  $J_{i,j}^{\text{AF}} = J_{\parallel}^{\text{AF}}$  if  $i$  and  $j$  are NN sites in the same layer (with same  $z$  coordinate), and  $J_{i,j}^{\text{AF}} = J_{\perp}^{\text{AF}}$  if  $i$  and  $j$  are NN sites belonging to two adjacent layers. In the third term,  $\phi_i$  corresponds to a site-dependent Coulomb potential that originates from the charge transfer through the interface, and it is determined via the Poisson equation as described below.  $W_i$  denotes the work function on either side, which is determined by the positions of the chemical potentials in the corresponding bulk materials. More details on  $\phi_i$  and  $W_i$  will be discussed later in this section.  $n$  is the  $e_g$  charge density. The fourth term stands for the electron-phonon coupling. The  $Q$ s are lattice distortions for the Jahn-Teller modes ( $Q_2$  and  $Q_3$ ) and breathing mode ( $Q_1$ ).  $\tau = (\tau^x, \tau^y, \tau^z)$  is the orbital pseudospin operator. The last term is the elastic energy of the lattice distortions considered here. The extra factor 2 for the breathing mode suppresses this mode as compared with the Jahn-Teller modes that are the most active.<sup>21</sup>

For any given  $t_{2g}$ -spin and lattice configuration the above Hamiltonian can be solved by numerically diagonalizing the bilinear fermionic sector. The ground state is approached via a relaxation technique: the optimized configuration of the oxygen coordinates and the  $t_{2g}$  spins is determined by minimizing the total energy of the Hamiltonian Eq.(1). This method is first applied to a  $4 \times 4 \times 4$  lattice with periodic boundary conditions to estimate properties of the bulk compound on each side of the heterostructure. In this publication, we will focus on the interface between an A-AFM and a G-AFM. Hence, we will adopt a set of parameters  $J^{\text{AF}}$  and  $\lambda$  that gives A-AFM and G-AFM ground states at the limits of  $e_g$  electron densities  $n = 1$  and  $n = 0$ , respectively. The same set of parameters is then used to calculate the ground state of the heterostructure. The heterostructure is defined on a  $4 \times 4 \times 8$  lattice (see Fig. 1), with periodic boundary conditions in the  $xy$  plane ( $ab$  plane) and open boundary conditions along the  $z$  direction ( $c$  axis). The initial spin configuration is set to be A-AFM on one side of the heterostructure (4 layers) with electron density  $n = 1$ , and G-AFM on the other side (4 layers) with  $n = 0$ . Regarding the relative spin direction between the A-AFM and G-AFM states, their relative angles  $\theta$  and  $\phi$  were allowed to take 16 equally-spaced values in their respective ranges, i.e.  $[0, \pi]$  for  $\theta$  and  $[0, 2\pi]$  for  $\phi$ , thus giving 256 possibilities. For each of these 256 possibilities, and a fixed set of couplings in the Hamiltonian, an independent optimization of the classical variables was made, namely the energy was minimized by solving

$$\nabla_{\psi_i} \langle H_{2b} \rangle = 0 \quad (2)$$

self-consistently using the Broyden's method,<sup>22</sup> where  $\psi_i = (\theta_i, \varphi_i, Q_{1i}, Q_{2i}, Q_{3i})$ . At each step we keep the two end layers to be dominated by the A-AFM and G-AFM states, respectively. Namely, the dominant layer wavevector for the Fourier transform of the spin-spin cor-

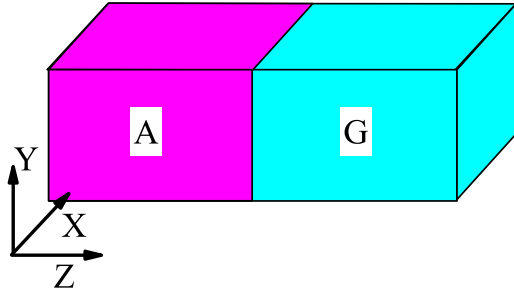


FIG. 1: Schematic representation of the heterostructure studied in this paper. It is defined on a  $4 \times 4 \times 8$  lattice. The bulk material on one side of the heterostructure is in the A-AFM phase, while the bulk material on the other side is in the G-AFM phase.

relations must be  $(0,0)$  and  $(\pi,\pi)$ , respectively, otherwise the configuration is discarded. The rest of the layers, of course, may have different magnetic orders. The optimized spins and oxygen coordinates of the ground state then corresponds to the configuration with the lowest overall energy after this long optimization process.

The charge transfer through the interface is taken into account via the self-consistent solution of the Coulomb potential  $\phi_i$ .<sup>3</sup> For the heterostructure discussed here, involving manganites only, we assume  $W_A = W_G$  and make them equal to zero for simplicity. This approximation is in agreement with results of previous discussions.<sup>5</sup> Then, the charge transfer through the interface is fully driven by the charge density difference, i.e., the charge always transfers from the A-AFM side to the G-AFM side. To properly describe the charge transfer, the long-range Coulomb interaction among the mobile  $e_g$  electrons and the positively charged ionic background must be included into the Hamiltonian as

$$H_{\text{Coul}} = \alpha t_0 \sum_{i \neq j} \left[ \frac{1}{2} \frac{n_i n_j}{|\vec{r}_i - \vec{r}_j|} - \frac{n_i n_j^+}{|\vec{r}_i - \vec{r}_j|} \right], \quad (3)$$

where  $\alpha = e^2/\epsilon a t_0$  is a dimensionless screening parameter. For manganites, it is known that  $t_0$  is of the order of 0.5 eV and the lattice constant  $a \approx 4\text{\AA}$ , hence  $\alpha$  depends on the choice for the dielectric constant  $\epsilon$ . However,  $\epsilon$  is both temperature and frequency dependent and for this reason an accurate estimation of  $\alpha$  is not well known. In this paper, the Hamiltonian Eq.(3) is studied over a broad range of  $\epsilon$  values,  $2 \leq \epsilon \leq 20$ , corresponding to  $0.2 \leq \alpha \leq 2$ .  $\vec{r}_i$  is the position vector of the Mn site  $i$ .  $n_i$  is the local electronic density at site  $i$ .  $n_i^+$  stands for the effective positive charge density on the  $i$ -th Mn site arising from the background ions. Note that to simplify the model, we have already assumed that all the charges from the background ions are located on the Mn

sites. Therefore, for the RMO/AMO heterostructure,  $n_i^+$  is fixed to 1 at the A-AFM side, and to 0 at the other side to enforce the charge neutrality.

Equation 3 is solved at the mean-field level by introducing the Coulomb potential

$$\phi_i = \sum_{j \neq i} \frac{\langle n_j \rangle - n_j^+}{|\vec{r}_i - \vec{r}_j|}. \quad (4)$$

We then find that the Coulomb interaction in Eq.(3) recovers the third term in Eq.(1). In practice, the Coulomb potential  $\phi_i$  is determined at each step of the relaxation procedure by self-consistently solving the Poisson's equation

$$\nabla^2 \phi_i = \alpha (\langle n_i \rangle - n_i^+). \quad (5)$$

Numerically the following discretization is applied:  $\partial^2 \phi / \partial x^2 = \phi_{i+\hat{x}} - 2\phi_i + \phi_{i-\hat{x}}$ ,  $\partial^2 \phi / \partial y^2 = \phi_{i+\hat{y}} - 2\phi_i + \phi_{i-\hat{y}}$ , and  $\partial^2 \phi / \partial z^2 = \phi_{i+2\hat{z}} - 2\phi_{i+\hat{z}} + \phi_i$ . The open boundary condition is applied along the  $z$  direction (out-of-plane) but periodic boundary conditions are applied along the  $x$  and  $y$  directions (in-plane).

In this work, up to 4,000 iterations per set of couplings (an iteration here is defined as an update of the entire set of classical variables in the cluster) are used to obtain the optimized spin and oxygen lattice configurations of the ground state. The most typical number of iterations is approximately 1,000. At each iteration of this relaxation procedure, up to 2,000 additional iterations at a fixed set of classical variables are used to solve the Poisson's equation. Note that the diagonalization of fermions must be performed at each step in solving this Poisson's equation. Then, in order to find the optimized configuration for the ground state on a  $4 \times 4 \times 8$  lattice, typically approximately  $10^6$  times the exact diagonalization of the  $256 \times 256$  matrix is necessary. This is very CPU time demanding. It is for these practical reasons that only the  $4 \times 4 \times 8$  lattice is used here to study the properties of the heterostructure.

### III. RESULTS FOR NARROW TO INTERMEDIATE BANDWIDTH MANGANITES

In this section, results for the RMO/AMO heterostructure will be discussed, where (R,A)MO corresponds to a narrow-to-intermediate bandwidth manganite, such as (La, Ca)MnO<sub>3</sub> and (Pr, Ca)MnO<sub>3</sub>. Therefore, the results presented here are expected to best describe the properties of LaMnO<sub>3</sub>/CaMnO<sub>3</sub> or PrMnO<sub>3</sub>/CaMnO<sub>3</sub> heterostructures.

#### A. Phase diagram of the bulk material

Before discussing the properties of the heterostructure, we will first analyze the magnetic phase diagram of the

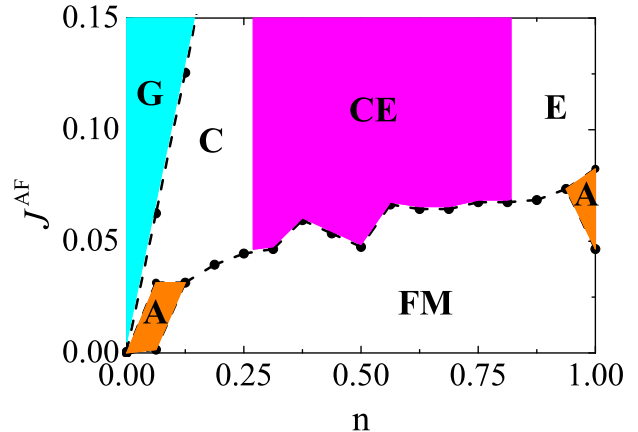


FIG. 2: Phase diagram of the two-orbital model on the  $4 \times 4 \times 4$  cubic lattice with  $J_{\parallel}^{\text{AF}} = J_{\perp}^{\text{AF}} = J^{\text{AF}}$  and  $\lambda = 1.5$ . The results are obtained comparing the energies of the G-AFM, C-AFM, CE-AFM, E-AFM, A-AFM, and FM states.

corresponding bulk material. On one hand, this allows us to determine the model parameters to be used for the calculation of heterostructures; on the other hand, a better knowledge of the bulk phase diagram also helps in understanding the possible spin structures in the heterostructure.

Previous theoretical investigations<sup>20</sup> have shown that in the two-orbital model the bandwidth depends on the electron-phonon coupling strength  $\lambda$  and the superexchange coupling strength  $J^{\text{AF}}$ . The larger the  $\lambda$  and  $J^{\text{AF}}$  are, the narrower the bandwidth is. In Fig. 2 the phase diagram of the two-orbital model for the bulk is shown at various electronic densities, using  $\lambda = 1.5$  and  $J_{\parallel}^{\text{AF}} = J_{\perp}^{\text{AF}} = J^{\text{AF}}$ . The phase diagram is obtained by comparing energies of several candidate states: A-AFM, G-AFM, C-AFM, E-AFM, CE-AFM, and FM states on the  $4 \times 4 \times 4$  lattice. Note that there could exist even more exotic states in the phase diagram, such as the  $C_x E_{1-x}$  state previously proposed<sup>23</sup> at  $n > 0.5$  if larger lattice sizes could be considered, and spiral states at  $n = 1$  when in the presence of spin frustration.<sup>24</sup> However, as shown below our interest will be mainly in the A-AFM state stabilized at electronic density  $n = 1$ , the CE and A-AFM states at  $n = 0.5$ , and the G-AFM state at  $n = 0$ , namely in regions where the  $C_x E_{1-x}$  and spiral states are not expected to be relevant. Hence in the current study, the  $C_x E_{1-x}$  and spirals states are not considered.

The bulk phase diagram is very rich. At small superexchange couplings the ground state is FM in a broad density regime, as expected from the double-exchange mechanism. At larger superexchange coupling the system transitions, from low to high electronic densities, from G-AFM, to C-AFM, to CE-AFM, and finally to E-AFM phases, respectively. Close to  $n = 0.5$  the CE phase

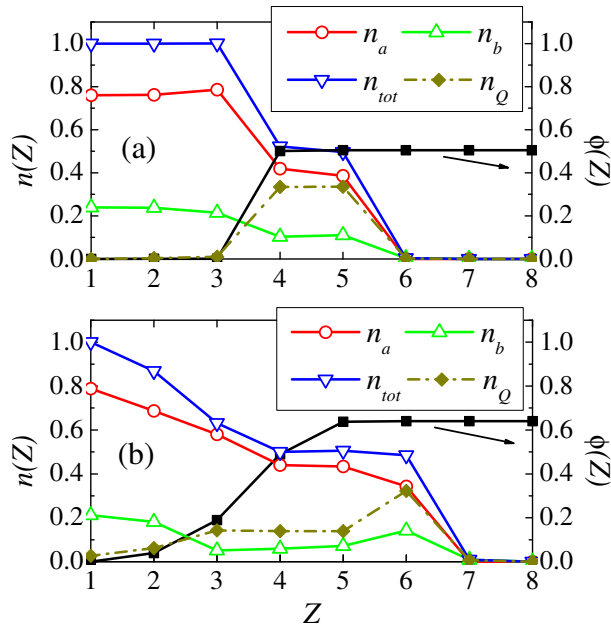


FIG. 3: Layer-averaged electronic density  $n(Z)$  and electrostatic potential  $\phi(Z)$ , at  $\lambda = 1.5$  and  $J^{\text{AF}} = 0.065$ , vs. layer index.  $n_a$  and  $n_b$  refer to the electronic densities of the  $a$  and  $b$  orbitals, and  $n_{\text{tot}} = n_a + n_b$ ,  $n_{\mathbf{Q}}$  is the Fourier transform of the local electronic density in each layer at  $\mathbf{Q} = (\pi, \pi)$ . (a) are results at  $\alpha = 1.0$ ; (b) are results at  $\alpha = 0.3$ .

is stable over a wide range of  $J^{\text{AF}}$  values and has an alternate charge/orbital order; whereas the G-AFM phase at low  $n$  has neither charge nor orbital order. There are also two A-AFM phases: close to electronic density  $n = 1$  at intermediate  $J^{\text{AF}}$  and close to  $n = 0$  at small  $J^{\text{AF}}$  values. The one close to  $n = 1$  has the correct alternate  $3x^2 - r^2/3y^2 - r^2$  orbital order expected at  $n = 1$  from experimental information.<sup>21,25</sup> Thus, it is interesting to point out that in the range  $0.05 \leq J^{\text{AF}} \leq 0.075$  the phase diagram consists of G-AFM, C-AFM, CE, FM, and A-AFM phases consecutively from low to high electronic densities, correctly resembling the phase diagram of real narrow-to-intermediate bandwidth bulk manganites.<sup>26</sup> Hence,  $J_{\parallel}^{\text{AF}} = J_{\perp}^{\text{AF}} = 0.065$  and  $\lambda = 1.5$  will be used as couplings for calculations of the heterostructures to be discussed later in this section.

## B. CE state close to the interface of the heterostructure

### 1. Emergence of CE properties near the interface

In this subsection, the physical properties of the heterostructure are investigated using the above described model parameters. In Fig. 3, the averaged electronic den-

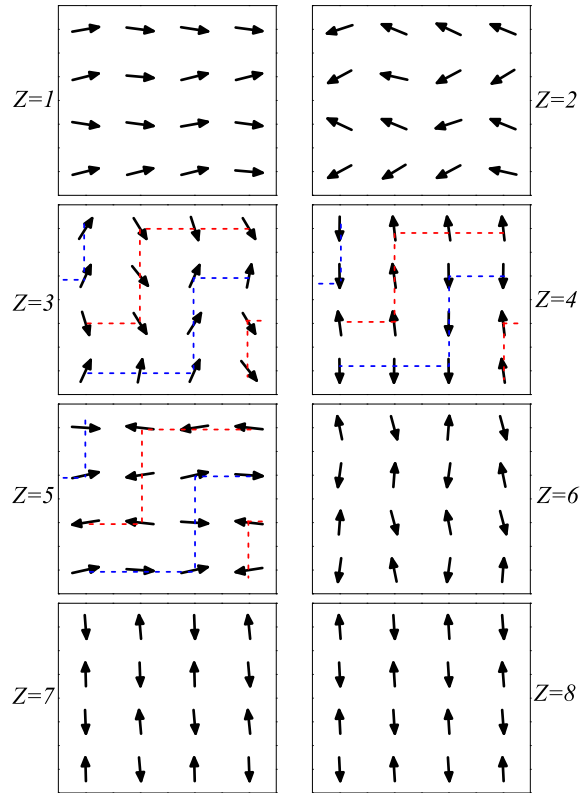


FIG. 4: Optimized spin configurations of the heterostructure studied here, using  $\lambda = 1.5$ ,  $J^{\text{AF}} = 0.065$ , and  $\alpha = 1.0$ . The dashed lines highlight the spin zigzag chains that are characteristic of CE states, with FM order within each chain.

sity  $n(Z)$  and electrostatic potential  $\phi(Z)$  in each layer are presented at  $\alpha = 1.0$  and  $\alpha = 0.3$ . At the two end layers of the heterostructure, the densities  $n(Z = 1) \approx 1$  and  $n(Z = 8) \approx 0$  converge to the expected values in the corresponding bulk materials. But charges are redistributed in the rest of the layers due to the long-range Coulomb interactions. Note that there exists a plateau at  $n_{\text{tot}}(Z) \approx 0.5$  in the layers close to the interface. To understand this feature, let us study the Fourier transform of the local electronic density in each layer,  $n_{\mathbf{Q}} = \frac{1}{N_{\text{XY}}} \sum_i n_i e^{i\mathbf{Q} \cdot \mathbf{r}_i}$ , where  $N_{\text{XY}}$  is the number of sites in each layer.  $n_{\mathbf{Q}}$  at  $\mathbf{Q} = (\pi, \pi)$  displays a peak in the layers close to the interface, where the plateau in  $n_{\text{tot}}$  exists. This suggests the presence of a charge ordered phase with  $n_{\text{tot}}(Z) \approx 0.5$  that is stabilized at the interface. Such a charge ordered state is found to appear at the interface for all the  $\alpha$  values considered in our study. Hence, we believe the existence of this state is an intrinsic property at the interface of the heterostructure, at least within the approximations used in our calculations.

To better understand the states that are located at or close to the interface, it is important to study how the

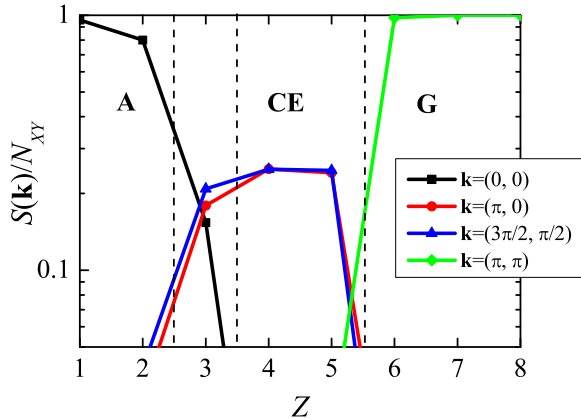


FIG. 5: Layer dependence of the spin structure factor  $S(\mathbf{k})$  for the optimized spin configurations shown in Fig. 4 at several momenta  $\mathbf{k}$ :  $(0, 0)$ ,  $(\pi, 0)$ ,  $(3\pi/2, \pi/2)$ , and  $(\pi, \pi)$ .

spins are ordered in each layer of the heterostructure. We have observed that the spin order is not much sensitive to the value of  $\alpha$ .<sup>27</sup> Thus, here only the information for the optimized real-space spin patterns at  $\alpha = 1.0$  is presented in Fig. 4. From this figure, it is clear that the layers close to the interface (layers 3, 4, and 5) exhibit a CE-type spin order. It is well known that in bulk systems and narrow bandwidth manganites, the CE state is stabilized at electronic density  $n \approx 0.5$  and has a staggered charge order. Moreover, our previous results in this section using a cubic cluster to mimic the bulk also unveiled a CE state at the same density. Thus, the CE spin order found here further confirms that a charge/spin/orbital ordered state is stabilized at the interface.<sup>28</sup>

Moving from the interface towards one end of the heterostructure (layer 1), the CE state gives way to the FM order in each layer. But spins in two adjacent layers tend to be AFM coupled, see layers 1 and 2 for instance. Hence, the state at this end of the heterostructure has an A-AFM tendency, resembling the spin order in the bulk. Similarly, the state on the other side of the heterostructure turns from the CE state to a G-AFM. The above described features are further confirmed by the layer-dependent spin structure factor  $S(\mathbf{k}) = \frac{1}{N_{XY}} \sum_{i,j} \mathbf{S}_i \cdot \mathbf{S}_j e^{i\mathbf{k} \cdot (\mathbf{r}_i - \mathbf{r}_j)}$  shown in Fig. 5. Considering the degeneracy of states with ordering vector  $\mathbf{k} = (\pi, 0)$  and  $(0, \pi)$ , and with  $\mathbf{k} = (\pi/2, 3\pi/2)$  and  $(3\pi/2, \pi/2)$ , the CE order in layers 4 and 5 is nearly perfect.

## 2. Novel states at the interface with no bulk analog in experimentally known phase diagrams

The previous analysis shows that the interface has CE characteristics. This may be considered as an “obvious”

result, since in a heterostructure the interpolation between bulk materials with  $n = 1$  and  $n = 0$  likely will induce  $n = 0.5$  at the interface. In this simplistic conceptual framework, the properties at the interface can be guessed, with good accuracy, merely from the bulk phase diagram. While this provides a reasonable starting point to analyze results and make predictions, further analysis actually suggests that this is not the end of the story, and some surprises can be unveiled at interfaces.

To illustrate this point, consider for instance layer 3. Here, the average density is very close to 1, yet the spins form zigzag chains as in the CE state of  $n = 0.5$ . The reason is that the spins at layer 3 are already being influenced by the robust CE state formed at layer 4. Thus, layer 3 is an exotic interpolation between the extremes case of the FM layers of the A-AFM state in one end, and the CE state at the interface. Moreover, note that the relative orientation between the spins of adjacent zigzag chains of layer 3 is not antiferromagnetic, as in a normal CE state, but it has some canting. This “canted CE state” is not present in bulk phase diagram, to our knowledge. Note that a state called the “pseudo CE” was previously discussed in experiments.<sup>29</sup> Considering just the individual layers, this state is the same as the usual CE, but the coupling between CE layers is ferromagnetic, instead of antiferromagnetic as in the standard CE state. Thus, this pseudo CE state is not the same observed in our heterostructures. Also note that a “canted CE” state similar to that described in the present investigations was reported in early neutron diffraction experiments<sup>30</sup> of  $\text{Pr}_{0.7}\text{Ca}_{0.3}\text{MnO}_3$ . However, further investigations for the same material<sup>29,31</sup> suggested instead a mixed-phase interpretation of the results, with a mixture of AF and FM phases, as opposed to a uniform canted CE state. Thus, to our knowledge there is no evidence that the canted CE state exists in bulk form in real experiments, although more work is needed to fully address this matter. Also we are not aware of previous theoretical investigations reporting such a canted CE state.<sup>32</sup>

We also noticed that although the layers located right at the interface, i.e. layers 4 and 5, exhibit almost a perfect CE order individually, the spins in the two layers are not perfectly AFM aligned with respect to one another compared with what they should be in a bulk CE phase. In other words, the CE state in the bulk is well known for showing a “stacking” property along the direction perpendicular to the CE plane, which is respected here with regards to charge and orbital but not with respect to the AFM relative order of the spins. In fact, in the layers  $Z=4$  and  $5$  of the heterostructure, the relative spin orientation is at approximately  $90^\circ$  degrees, namely they are spin perpendicular to one another. Once again, to our knowledge such an arrangement does not exist in the bulk. While it is obvious that the interplane spin deviation from AFM order in a CE arrangement will increase the superexchange energy of the system, these spin arrangements also allow for charge transferring out-of-plane. In other words, having an AFM order in a

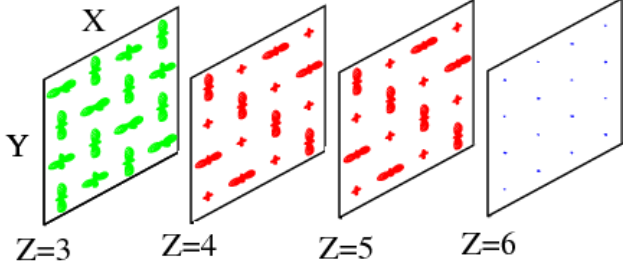


FIG. 6: Real-space orbital pattern of the  $e_g$  electrons for the layers close to the interface. The model parameters are the same as in Fig. 4. The radial part of the electron wave function (shown) is proportional to the local  $e_g$  electronic density  $n_i$ . The plot displays a transition from the staggered  $3x^2 - r^2/3y^2 - r^2$  order in layer 3, to a CE-type orbital order in layers 4 and 5, and then to a weak  $3z^2 - r^2$  order in layer 6, consistent with the spin patterns in Fig. 4.

link reduces the effective hopping amplitude to zero in a double-exchange context. But if the spin order is not AFM, the kinetic energy in that link improves. Then, the system can gain double exchange energy in the  $z$  direction at the expense of superexchange if the CE stacking does not involve AFM order. As a combined effect, the total energy appears to be lowered by this mechanism at the interfaces we studied here, while in the bulk it does not occur.

The charge distribution in Fig. 3 suggests that on average the  $a$  ( $x^2 - y^2$ ) orbital has a higher occupation number than the  $b$  ( $3z^2 - r^2$ ) orbital. To obtain the exact orbital pattern at each site, the expectation values of the local pseudo-spin operators  $\langle \tau_i^x \rangle$  and  $\langle \tau_i^z \rangle$  are calculated. Defining an effective phase angle  $\xi_i = \pi + \tan^{-1}(\langle \tau_i^x \rangle / \langle \tau_i^z \rangle)$ , we introduce a dressed state  $|b\rangle = \left[ -\sin(\xi_i/2)c_{ia}^\dagger + \cos(\xi_i/2)c_{ib}^\dagger \right] |0\rangle$  from which the orbital occupation is computed as  $\langle b|n_i|b\rangle$ . The details of this type of calculations are well-known and they can be found in Ref. 33.

To discuss the orbital pattern explicitly, let us focus on the optimized configuration with model parameters  $\lambda = 1.5$ ,  $J^{\text{AF}} = 0.065$ , and  $\alpha = 1.0$ . For other  $\alpha$  values the patterns look very similar. The orbital patterns in layers 1 and 2, where the bulk-like A-AFM phase is stabilized, display a clear staggered  $3x^2 - r^2/3y^2 - r^2$  order. Reciprocally, layers 7 and 8 do not show any orbital order due to the vanishing value of the electronic density. However, the orbital patterns close to the interface in the range of layers from 3 to 6 are complicated and they are presented in Fig. 6. Here, we observe a transition from the staggered  $3x^2 - r^2/3y^2 - r^2$  order to the orbital order of the CE state, and then to a (very weak)  $3z^2 - r^2$  order in the G-AFM state, with increasing layer index. In layer 3, the orbital pattern is very close to that expected of a  $n = 1$  state, but note that the orbital population

along one of the orientations of the diagonals is not identical for each diagonal. This is caused by the influence of the CE state of the layer 4. In addition, in the CE state of layers 4 and 5, the “bridge” sites, which have a higher electronic density than the rest, have staggered  $3x^2 - r^2/3y^2 - r^2$  order, but the “corner” sites show a uniform  $x^2 - y^2$  order, which is larger than in the CE state stabilized in the bulk. In general, we find that in layers where either FM or CE spin order exist the  $e_g$  electrons prefer to form an in-plane orbital order. This is because in these layers the two oxygens connected to a Mn ion tend to shrink along the  $z$  direction to minimize the energy of electron-phonon interactions by decreasing  $Q_3$ . But in the layers where there is a G-AFM state, the oxygens will expand along the  $z$  direction to partially compensate the shrinking effect along this direction in other layers.<sup>34</sup> Hence, a  $3z^2 - r^2$  order may appear. In summary, the features of the orbital arrangements are dominated by what we expect to find in  $n = 1$  A-AFM,  $n = 0.5$  CE, and  $n = 0.0$  G-AFM states. However, subtle deviations can be observed: non equivalent diagonals in layer 3, corner population in the zigzags of layers 4 and 5, and weak orbital occupation along the  $z$ -axis in layer 6.

#### IV. RESULTS FOR WIDE BANDWIDTH MANGANITES

In the previous section, the physical properties of the  $\text{LaMnO}_3/\text{CaMnO}_3$  and  $\text{PrMnO}_3/\text{CaMnO}_3$  heterostructures were discussed. States with CE characteristics were found to be stabilized near the interface. But for the cases of the  $\text{LaMnO}_3/\text{SrMnO}_3$  and  $\text{PrMnO}_3/\text{SrMnO}_3$  heterostructures, we expect to obtain different interfacial states because the corresponding bulk materials, such as  $(\text{La, Sr})\text{MnO}_3$  and  $(\text{Pr, Sr})\text{MnO}_3$ , have a wider bandwidth and the CE state is not stabilized in these compounds at half doping.

##### A. The bulk phase diagram

As in the previous section, let us first study the phase diagram of the wide bandwidth manganite in bulk form, focusing here on the case  $\lambda = 1.2$ . This coupling is smaller than the one used for narrow bandwidth manganites. However, for  $J_{\parallel}^{\text{AF}} = J_{\perp}^{\text{AF}} = J^{\text{AF}}$ , as shown in Fig. 7(a), the A-AFM phase at  $\lambda = 1.2$  cannot be stabilized near  $n \approx 1$ . This is because the A-AFM phase only appears in a very narrow regime of the phase diagram in the two-orbital model if a cubic lattice symmetry is considered.<sup>23</sup> This is compatible with the fact that the real compounds exhibiting the A-AFM phase, such as  $\text{LaMnO}_3$ , have an orthorhombic, instead of cubic, lattice symmetry, with the lattice constant along the  $c$  axis smaller than those along the  $a$  and  $b$  axes.<sup>35</sup> To better incorporate the lattice distortion found in the

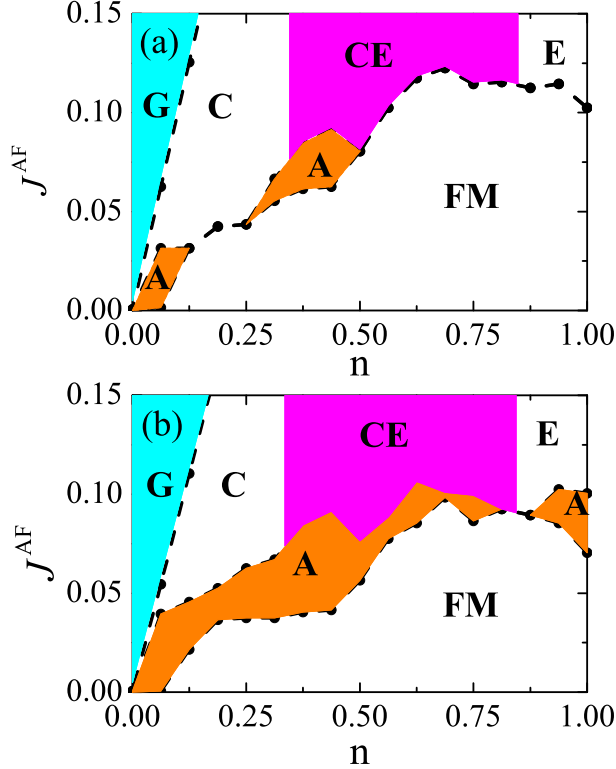


FIG. 7: Phase diagram of the two-orbital model on the  $4 \times 4 \times 4$  lattice with  $\lambda = 1.2$ . Shown are the cases: (a)  $J_{\parallel}^{\text{AF}} = J_{\perp}^{\text{AF}} = J^{\text{AF}}$ , and (b)  $J_{\parallel}^{\text{AF}} = 2J_{\perp}^{\text{AF}}/3 = J^{\text{AF}}$ . The results were obtained comparing the energies of the states G-AFM, C-AFM, CE-AFM, A-AFM, E-AFM, and FM.

bulk parent compound, an inter-layer superexchange coupling larger than the intra-layer one should be used, i.e.  $J_{\perp}^{\text{AF}} > J_{\parallel}^{\text{AF}}$ .<sup>14,21</sup> The ratio  $J_{\perp}^{\text{AF}}/J_{\parallel}^{\text{AF}}$  is estimated<sup>14,21,36</sup> to be  $1.2 \sim 1.5$ . Using these numbers, the phase diagram for  $J_{\parallel}^{\text{AF}} = 2J_{\perp}^{\text{AF}}/3 = J^{\text{AF}}$  at  $\lambda = 1.2$  is shown in Fig. 7(b). The A-AFM phase is now stabilized in a wider regime of the phase diagram, including  $n \approx 1$ . Thus, tuning  $J^{\text{AF}}$  to 0.07, the system experiences transitions involving the G-C-A-FM-A phases with increasing electronic density  $n$ , and this resembles properly the experimentally observed phases of wide-bandwidth manganites (R, A)MO.<sup>26</sup>

As for the RMO/AMO heterostructure, the state on each side, far from the interface, must converge to its bulk phase. To obtain a stable A-AFM phase in the bulk RMO, we use the couplings  $\lambda = 1.2$  and  $J_{\parallel}^{\text{AF}} = 2J_{\perp}^{\text{AF}}/3 = J^{\text{AF}} = 0.07$  on the RMO side of the heterostructure. On the AMO side, since the bulk AMO still has the cubic lattice symmetry,<sup>13</sup> we adopt  $\lambda = 1.2$  and  $J_{\parallel}^{\text{AF}} = J_{\perp}^{\text{AF}} = J^{\text{AF}} = 0.07$ . At the interface, the lattice constants along the  $a$  and  $b$  axes will compress but those along the  $c$  axis elongate to recover the cubic

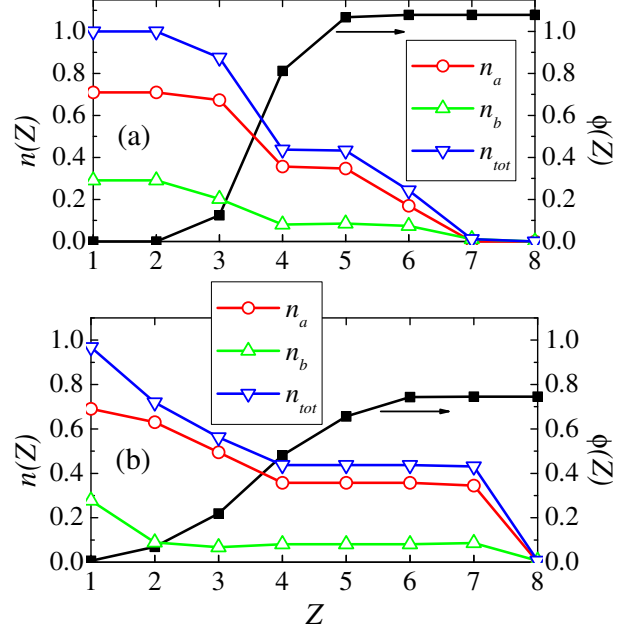


FIG. 8: Layer-averaged electron density  $n(Z)$  and electrostatic potential  $\phi(Z)$ , obtained using  $\lambda = 1.2$  and  $J^{\text{AF}} = 0.07$ .  $n_a$  and  $n_b$  refer to the electron densities of the  $a$  and  $b$  orbitals, and  $n_{\text{tot}} = n_a + n_b$ . (a) are results for  $\alpha = 1.0$ ; (b) are results for  $\alpha = 0.2$ .

symmetry due to the strain effect. Thus, we adopt the inter-layer superexchange coupling  $J_{\perp}^{\text{AF}} = J^{\text{AF}} = 0.07$  at the interface.

## B. The state at the interface of the heterostructure

The averaged electrostatic potential and electronic densities in each layer at  $\alpha = 1.0$  and  $\alpha = 0.2$  are presented in Fig. 8. These charge distributions are actually similar to those shown in Fig. 3. Interestingly, there is also a plateau at  $n \approx 0.5$  indicating the existence of a fairly stable half-doped state near the interface. Although there is no CE phase in the phase diagram of wide bandwidth manganites, we find instead that the A-AFM phase can be stabilized at  $n \approx 0.5$  in the bulk limit. Thus, the plateau at  $n \approx 0.5$  in Fig. 8 suggests the state at the interface to be the A-AFM state. This assumption is fully supported by the optimized real-space spin configuration results presented in Figs. 9 and 10: for both  $\alpha = 1.0$  and  $\alpha = 0.2$ , the A-AFM phase spin arrangement is found in layers close to the interface.

Figures 9 and 10 indicate that the transition from the A-AFM state at the interface to the G-AFM state at one end of the heterostructure depends on the value of the screening parameter  $\alpha$ . At a large  $\alpha$  value, an interesting result is found. In this case, there is one layer (layer 6)

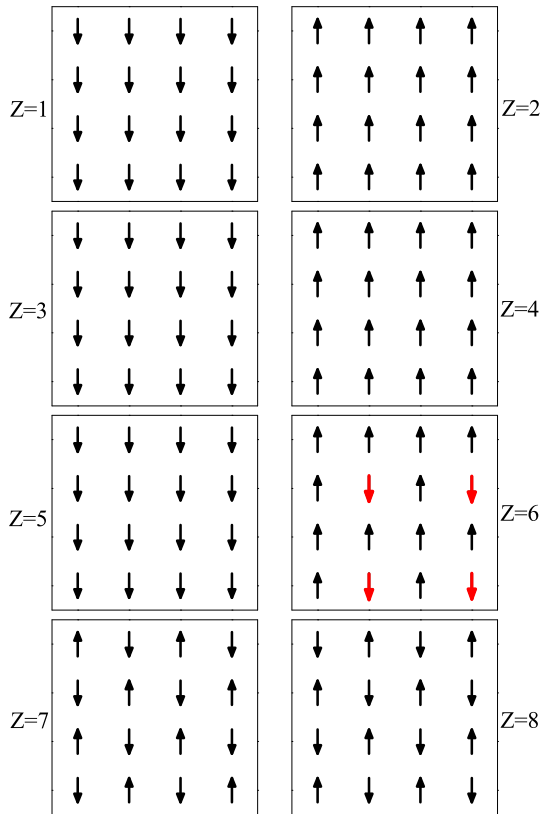


FIG. 9: The optimized real-space spin configuration at each layer of the heterostructure with the model parameters used in Fig. 8(a).

with an intermediate exotic state, that has no analog in the bulk experimental phase diagrams, to our knowledge. This state consists of alternate FM and AFM stripes, indicating a local mixed phase tendency. Note that we have carried out numerical studies on square clusters,  $\lambda = 1.2$ , and  $J^{\text{AF}} = 0.07$ , simulating bulk two dimensional systems, and in this case we do find a similar mixed AF-FM state at electronic quarter-filling densities. Thus, it is conceivable that this state may exist in bulk single-layer manganites at large hole doping as well. At small  $\alpha$  values, on the other hand, the transition is via introducing spin canting in several layers. We note that in real heterostructures, the mixed-phase tendencies and spin canting may coexist.

Let us consider now the orbital occupation near the interface. In Fig. 11 the orbital pattern near the interface for  $\lambda = 1.2$ ,  $J^{\text{AF}} = 0.07$ , and  $\alpha = 1.0$  is presented. It is interesting to observe that the orbital pattern shows a clear transition from a staggered  $3x^2 - r^2/3y^2 - r^2$  order at one end of the heterostructure to a uniform  $x^2 - y^2$  order at the interface, layers 4 and 5, although the spin order is unchanged and fixed into an A-AFM state. This

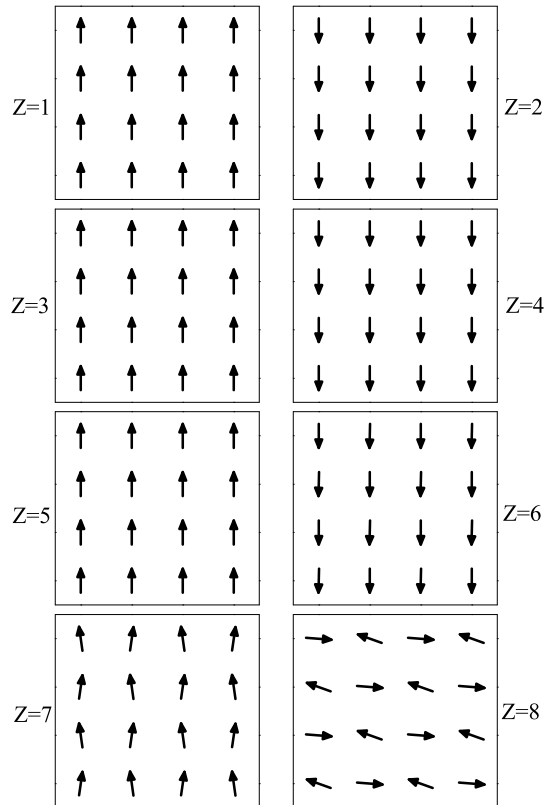


FIG. 10: The optimized real-space spin configuration at each layer of the heterostructure with the model parameters used in Fig. 8(b).

is understandable, since we know in the bulk the A-AFM exists both close to  $n = 1$  and close to  $n = 0.5$ . Comparing with Fig. 8(a), we observe that the orbital order is tightly connected to the average electronic density of the layer: the  $3x^2 - r^2/3y^2 - r^2$  order appears at  $n \approx 1$ , but the  $x^2 - y^2$  order is present at  $n \approx 0.5$ . Such a uniform  $x^2 - y^2$  orbital order is also observed in the A-AFM phase at  $n \approx 0.5$  in the bulk material.<sup>33,37</sup> Since the bulk A-AFM phase at  $n \approx 0.5$  is metallic, the A-AFM state at the interface of the heterostructure can be anticipated to be a two-dimensional metal. However, note that such a 2D metallic state could be unstable due to Anderson localization introduced by the roughness and defects at the interface. Hence, an insulating behavior is more likely to be observed in real materials.

In the exotic layer 6 exhibiting the mixed AFM-FM tendency, the orbital pattern is complicated. According to Fig. 9, there are majority spins (black arrows in layer 6) and minority spins (red arrows). The minority spin sites correspond to  $3z^2 - r^2$  order. The sites adjacent to the minority spin sites display alternating  $3x^2 - r^2/3y^2 - r^2$  order, but the sites diagonal to the minority spin sites show a  $x^2 - y^2$  order. Once again,

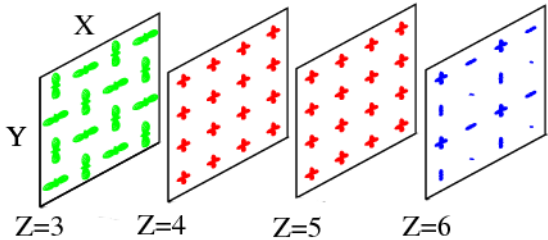


FIG. 11: The orbital pattern found in layers 3 to 6 of the heterostructure. A uniform  $x^2 - y^2$  orbital order is observed at the interface. The orbital order in layer 6 is exotic, i.e. not found in the bulk, similarly as the spin arrangement of the same layer.

we remark that such an exotic orbital order has not been observed experimentally in bulk materials to our knowledge, although it may be part of theoretical phase diagrams of models for two dimensional manganites in the bulk at large hole densities, and it is also conceivable that real single-layer manganites in the bulk may present also a similar phase.

## V. DISCUSSION AND CONCLUSIONS

In this paper, the magnetic and electronic properties of the states near the interface of RMO/AMO heterostructures were investigated using numerical optimization techniques on small clusters at zero temperature. The states stabilized at the interface are found to be similar to the states in the bulk compound at electronic density  $n \approx 0.5$ . This is easy to understand. Let us consider the superlattice  $(\text{RMO})_m/(\text{AMO})_n$ . When  $m, n \gtrsim a/\alpha$  where  $a$  is the lattice constant along the  $z$  direction, there must exist layers exhibiting properties of the bulk parent compounds RMO and AMO. In this case, the electronic density in the regime near the interface is not much sensitive to  $m$  or  $n$ , but is always close to 0.5 if  $\alpha$  is about the same on both sides of the heterostructure. Then, the regime close to the interface (within  $a/\alpha$  in the  $z$  direction) can accommodate the state stabilized at  $n \approx 0.5$  in the bulk. For the case of a wide bandwidth manganite, a uniformly  $x^2 - y^2$  ordered A-AFM phase is stabilized at the interface. Hence we propose that this state should exist in the long-period  $(\text{LMO})_m/(\text{SMO})_n$  superlattice where  $m$  and  $n$  are large enough such that there are bulk-like A-AFM and G-AFM insulating regimes far from the interface. It is quite reassuring that recent experiments on the  $(\text{LMO})_n/(\text{SMO})_{2n}$  superlattice at  $n = 3$  provided strong evidence for the existence of this orbital ordered A-AFM phase.<sup>13</sup> However, for short-period superlattices, the electronic density near the interface may deviate from 0.5, and also note that a well-defined bulk-like regime may not exist in these structures. Hence the state stabilized at the interface may be different from

the one in the long-period superlattice. For instance, in the  $(\text{LaMnO}_3)_{2n}/(\text{SrMnO}_3)_n$  superlattice with  $n < 4$ , the electronic density near the interface is always higher than 0.5,<sup>14</sup> falling into the FM regime in the phase diagram of bulk LSMO. Hence, it is natural to observe a metallic FM state stabilized at the interface.<sup>7,10,11,14,15</sup> Increasing the number of Sr layers, bulk-like insulating regimes appear and the superlattice is driven through the MIT to be an insulator. The electronic density at the interface is also reduced by increasing the number of Sr layers. As shown in Ref. 14, the state at the interface is still FM with a  $3z^2 - r^2$  orbital order. However, further increasing the number of Sr layers, the electronic density at the interface will approach 0.5. Then, the state at the interface becomes an A-AFM with a uniform  $x^2 - y^2$  orbital order as discussed above, and the properties of the heterostructure are dominated by bulk-like regimes.<sup>10</sup>

When studying the wide bandwidth manganites, we have used  $J_{\perp}^{\text{AF}} > J_{\parallel}^{\text{AF}}$ . For consistency, the same superexchange coupling ratio should be also used for the calculation of narrow-to-intermediate bandwidth manganites. But the A-AFM phase at  $n = 1$  is already stabilized in a cubic lattice for a large electron-phonon coupling. Thus, changing the superexchange coupling ratio does not modify the phase diagram crucially. Calculations have shown that setting  $J_{\perp}^{\text{AF}} > J_{\parallel}^{\text{AF}}$  also does not change the results for the heterostructures. Hence, we have only presented here the results with  $J_{\perp}^{\text{AF}} = J_{\parallel}^{\text{AF}}$  in Sec. III. In this case, interfaces dominated by CE-AFM characteristics have been observed.

It is very important to remark that several of our results have unveiled phases that are not observed in the bulk phase diagrams. They correspond to interesting modifications of the well-established bulk phases. For instance, for narrow bandwidth manganite heterostructures, the existence of exotic spin arrangements, such as ‘‘canted CE’’ and others, have been reported in our investigations. For wide bandwidth manganites, unexpected mixtures of FM and AF features were also identified. While our observations obtained on small clusters need to be confirmed by other many-body techniques, the present computational studies revealed the possibility of finding new phases at interfaces, that do not exist in the bulk. This is an exciting result that deserves further investigations. Figure 12 summarizes schematically our results.

Regarding size effects in our simulations, certainly it is possible that the actual spin, charge, and orbital patterns of the novel states may be more complicated than found in our present study that was limited to small systems. However, note that in the heterostructures discussed here the  $n = 1$  A-AFM on one side, the  $n = 0.5$  CE or A-AFM at the interface, and the  $n = 0$  G-AFM on the other side are very robust and likely will be present in real heterostructures. With these states (with different layer electronic density) anchored somewhere in the structure, then it is very reasonable to expect magnetic states *interpolating* between them, that will have novel

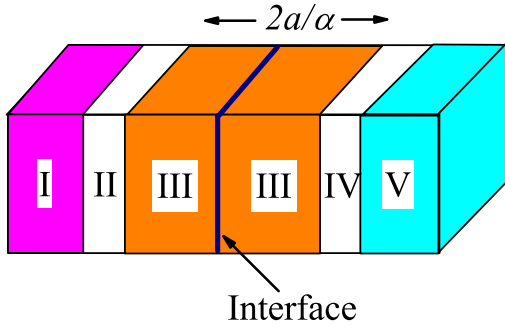


FIG. 12: Schematic representation of the results found in our investigations. I and V correspond to regions with properties similar to those of the bulk of the two materials involved in the heterostructures. Region III is very close to the interface. It is in this regime that the electronic density is approximately 0.5 if the bulk components have densities 1 and 0, as in our study. Depending on bandwidths here either a CE or an A-AFM state are found. Finally, in regions II and IV, the material must interpolate in properties between I and III or III and V. These interpolations lead to states that do not appear to have bulk analogs.

properties. In the bulk when the electronic concentration is the same in every layer of course it never happens that a magnetic layer must interpolate between others with different densities. Thus, we are confident that novel magnetic states, of a form likely even more complex than unveiled here, would be present in manganite superstructures if simulations using larger clusters were possible. Note that for bulk phase-separated manganites,<sup>20</sup> involving a competition between states with different electronic

densities, then the novel states discussed here could also appear at the interfaces between puddles of the competing phases as well.

In conclusion, we find that the properties of the RMO/AMO heterostructure are closely, but not entirely, associated with the phase diagram of the bulk compound (R, A)MO. We summarize our main results in Fig. 12. As one sees, although a uniform state does not exist in the heterostructure due to the redistribution of the charges, as a first approximation the state near the interface can be “read” from the phase diagram of the bulk compound (R, A)MO at electronic density  $n \approx 0.5$ , i.e., a CE state if (R, A)MO is a narrow-to-intermediate bandwidth manganite, but an A-AFM state with uniform  $x^2 - y^2$  orbital order if (R, A)MO is a wide bandwidth manganite. However, the intermediate states in between the interface and the bulk-like regimes are sensitive to both the model parameters and the length of the heterostructure. At least in our studies, it can be either a spin canted CE state or a state showing local FM-AF mixed tendencies. We believe our results can be used to describe the ground state properties of the long-period (RMO)<sub>m</sub>/(AMO)<sub>n</sub> superlattices as well.

## VI. ACKNOWLEDGMENT

We thank L. Brey, M. Daghofer, C. Lin, S. May, D. Khomskii, S. Okamoto, J. Salafranca, and Y. Tokura for useful discussions. This work was supported by the NSF under Grant No. DMR-0706020 and the Division of Materials Science and Engineering, U.S. DOE, under contract with UT-Battelle, LLC. S.Y. is also supported in part by CREST (JST).

<sup>1</sup> M. Izumi, Y. Murakami, Y. Konishi, T. Manako, M. Kawasaki, and Y. Tokura, Phys. Rev. B **60**, 1211 (1999).

<sup>2</sup> J. Chakhalian, J. W. Freeland, H.-U. Habermeier, G. Cristiani, G. Khaliullin, M. van Veenendaal, and B. Keimer, Science **318**, 1114 (2008).

<sup>3</sup> S. Okamoto and A. J. Millis, Phys. Rev. B **70**, 241104(R) (2004); S. Okamoto and A. J. Millis, Nature **428**, 630 (2004).

<sup>4</sup> J. Chaloupka and G. Khaliullin, Phys. Rev. Lett. **100**, 016404 (2008).

<sup>5</sup> S. Yunoki, A. Moreo, E. Dagotto, S. Okamoto, S. S. Kancharla, and A. Fujimori, Phys. Rev. B **76**, 064532 (2007).

<sup>6</sup> C. Lin and A. J. Millis, Phys. Rev. B **78**, 184405 (2008).

<sup>7</sup> C. Adamo, X. Ke, P. Schiffer, A. Soukiassian, M. Warusawithana, L. Maritato, and D. G. Schlom, Appl. Phys. Lett. **92**, 112508 (2008).

<sup>8</sup> H. Yamada, M. Kawasaki, T. Lottermoser, T. Arima, and Y. Tokura, Appl. Phys. Lett. **89**, 052506 (2006).

<sup>9</sup> B. R. K. Nanda and S. Satpathy, Phys. Rev. B **78**, 054427 (2008).

<sup>10</sup> S. J. May, A. B. Shah, S. G. E. te Velthuis, M. R. Fitzsimmons, J. M. Zuo, X. Zhai, J. N. Eckstein, S. D. Bader, and A. Bhattacharya, Phys. Rev. B **77**, 174409 (2008).

<sup>11</sup> Ş. Smadici, P. Abbamonte, A. Bhattacharya, X. Zhai, B. Jiang, A. Rusydi, J. N. Eckstein, S. D. Bader, and J.-M. Zuo, Phys. Rev. Lett. **99**, 196404 (2007).

<sup>12</sup> T. Koida, M. Lippmaa, T. Fukumura, K. Itaka, Y. Matsumoto, M. Kawasaki, and H. Koinuma, Phys. Rev. B **66**, 144418 (2002).

<sup>13</sup> A. Bhattacharya, X. Zhai, M. Warusawithana, J. N. Eckstein, and S. D. Bader, Appl. Phys. Lett. **90**, 222503 (2007).

<sup>14</sup> S. Dong, R. Yu, S. Yunoki, G. Alvarez, J.-M. Liu, and E. Dagotto, Phys. Rev. B **78**, 201102(R) (2008).

<sup>15</sup> A. Bhattacharya, S. J. May, S. G. E. te Velthuis, M. Warusawithana, X. Zhai, B. Jiang, J. M. Zuo, M. R. Fitzsimmons, S. D. Bader, and J. N. Eckstein, Phys. Rev. Lett. **100**, 257203 (2008).

<sup>16</sup> S. Yunoki, E. Dagotto, S. Costamagna, and J. A. Riera, Phys. Rev. B **78**, 024405 (2008); I. González, S. Okamoto,

- S. Yunoki, A. Moreo, and E. Dagotto, *J. Phys.: Condens. Matter* **20**, 264002 (2008).
- <sup>17</sup> L. Brey, *Phys. Rev. B* **75**, 104423 (2007).
- <sup>18</sup> M. J. Calderón, J. Salafranca, and L. Brey, *Phys. Rev. B* **78**, 024415 (2008); J. Salafranca, M. J. Calderón, and L. Brey, *Phys. Rev. B* **77**, 014441 (2008).
- <sup>19</sup> C. Lin, S. Okamoto, and A. J. Millis, *Phys. Rev. B* **73**, 041104 (2006).
- <sup>20</sup> E. Dagotto, T. Hotta, and A. Moreo, *Phys. Rep.* **344**, 1 (2001).
- <sup>21</sup> T. Hotta, S. Yunoki, M. Mayr, and E. Dagotto, *Phys. Rev. B* **60**, 15009(R) (1999).
- <sup>22</sup> W. H. Press, S. A. Teukolsky, W. T. Vetterling, and B. P. Flannery, *Numerical Recipes*, Vol. 1 (*2nd Ed.*, Cambridge University Press, 1992).
- <sup>23</sup> T. Hotta, M. Moraghebi, A. Feiguin, A. Moreo, S. Yunoki, and E. Dagotto, *Phys. Rev. Lett.* **90**, 247203 (2003).
- <sup>24</sup> S. Dong, R. Yu, S. Yunoki, J.-M. Liu, and E. Dagotto, *Phys. Rev. B* **78**, 155121 (2008).
- <sup>25</sup> Y. Murakami, J. P. Hill, D. Gibbs, M. Blume, I. Koyama, M. Tanaka, H. Kawata, T. Arima, Y. Tokura, K. Hirota, and Y. Endoh, *Phys. Rev. Lett.* **81**, 582 (1998).
- <sup>26</sup> R. Kajimoto, H. Yoshizawa, Y. Tomioka, and Y. Tokura, *Phys. Rev. B* **66**, 180402(R) (2002).
- <sup>27</sup> Although the spin order is not sensitive to the value of  $\alpha$ , the exact spin pattern does. This can be best seen from Fig. 9 and Fig. 10, where the relative angles between spins in layer 1 and layer 8 is different at different  $\alpha$ .
- <sup>28</sup> We remark that L. Brey in Ref. 17 also previously reported a charge-ordered CE state at the interface between a FM metal and a large-gap insulator, such as SrTiO<sub>3</sub>, due to a reduction of the electronic density at that interface.
- <sup>29</sup> D. E. Cox, P. G. Radaelli, M. Marezio, and S.-W. Cheong, *Phys. Rev. B* **57**, 3305 (1998). See also C. Yaicle, C. Martin, Z. Jirak, F. Fauth, G. Andri, E. Suard, A. Maignan, V. Hardy, R. Retoux, M. Hervieu, S. Hibert, B. Raveau, Ch. Simon, D. Saurel, A. Brulet, and F. Bouree, *Phys. Rev. B* **68**, 224412 (2003).
- <sup>30</sup> H. Yoshizawa, H. Kawano, Y. Tomioka, and Y. Tokura, *Phys. Rev. B* **52**, R13145 (1995).
- <sup>31</sup> P. G. Radaelli, R. M. Ibberson, D. N. Argyriou, H. Casalta, K. H. Andersen, S.-W. Cheong, and J. F. Mitchell, *Phys. Rev. B* **63**, 172419 (2001), and references therein. See also page 292 of Ref. 33.
- <sup>32</sup> In D. Efremov, J. van den Brink, and D. Khomskii, *Nature Mat.* **3**, 853 (2004), a modified CE state was discussed in the context of novel ferroelectric states. In this reference, the orientation of the spins within the zigzag chains is modified with respect to the pattern in the perfect CE state via the introduction of dimers. The state of Efremov *et al.* does not appear to be the same as in the “canted CE” state discussed in the present paper, but further work is needed to fully address this issue.
- <sup>33</sup> E. Dagotto, *Nanoscale Phase Separation and Colossal Magnetoresistance*, Springer Verlag, Berlin, 2002.
- <sup>34</sup> The compensation is not complete when considering the breathing mode in the model. In heterostructures, the periodicity of the lattice distortions along the  $z$  direction is lost so that the total volume of the lattice may not be kept constant due to the existence of the breathing mode.
- <sup>35</sup> J. Rodríguez-Carvajal, M. Hennion, F. Moussa, A. H. Moudden, L. Pinsard, and A. Revcolevschi, *Phys. Rev. B* **57**, R3189 (1998).
- <sup>36</sup> J. Zhou and J. Goodenough, *Phys. Rev. B* **77**, 132104 (2008).
- <sup>37</sup> R. Kajimoto, H. Yoshizawa, H. Kawano, H. Kuwahara, Y. Tokura, K. Ohoyama, and M. Ohashi, *Phys. Rev. B* **60**, 9506 (1999); A. Urushibara, Y. Moritomo, T. Arima, A. Asamitsu, G. Kido, and Y. Tokura, *Phys. Rev. B* **51**, 14103 (1995); Y. Tokura, A. Urushibara, Y. Moritomo, T. Arima, A. Asamitsu, G. Kido and N. Furukawa, *J. Phys. Soc. Jpn.* **63**, 3931 (1994).